Research Article | Vol. 16, No. 5 / 1 May 2025 / Biomedical Optics Express 1960
Biomedical Optics EXPRESS

Single-shot full-field optical coherence tomography with a single polarization camera

AHYEON HUR,[1,†] SUCBEI MOON,[2,†] YOUNG-WAN CHOI,[1,3] AND WOO JUNE CHOI[1,3,*]

[1]Department of Electrical and Electronics Engineering, Chung-Ang University, Seoul 06974, Republic of Korea
[2]Department of Physics, Kookmin University, Seoul 02707, Republic of Korea
[3]Department of Intelligent Semiconductor Engineering, Chung-Ang University, Seoul 06974, Republic of Korea
[†]The authors contributed equally to this work.
[*]cecc78@cau.ac.kr

Abstract: We present a novel implementation technique of single-shot full-field optical coherence tomography (S-FF-OCT) by utilizing a single-sensor polarization camera. S-FF-OCT is capable of acquiring interference image information in a single camera capture with a short signal integration time, which makes it particularly advantageous for tomographic imaging of fast-moving objects or samples under environmental vibrations. For a simple and compact system of S-FF-OCT, we developed a polarization-channeled detection scheme of interference based on a Linnik interferometer and a commercial polarization camera. The phase-shifted quadrature components of the polarized interferograms are generated by the polarization optics and can be analyzed using the polarization camera. A single capture of the interferograms yields an *en-face* OCT image with the help of the coherence gating effect. In this study, the imaging performance of our S-FF-OCT is validated by delineating moving objects and living biological specimens under ambient vibrations, thereby demonstrating its practical application potential for FF-OCT imaging *in situ*.

1. Introduction

Optical coherence tomography (OCT) is a low-coherence interferometry technique for three-dimensional (3D) imaging of topological and internal microstructures of scattering samples [1]. With advantages of non-invasive, label-free, high resolution imaging capabilities, OCT has been widely utilized as a non-destructive imaging tool across various fields, including biomedical [2] and industrial applications [3]. In particular, full-field optical coherence tomography (FF-OCT) [4], a variant of high-resolution OCT, has been of increased interest as a non-scanning, ultrahigh resolution *en face* imaging technology that is beneficial for morphologically and functionally examining sub-micrometer-scale structures such as cellular organelles [5].

Based on the working principle of low-coherence interferometry, FF-OCT typically retrieves sample information encoded in interference signal using phase-shifting interferometry [4,6], in which quadrature phase-shifted interference images of the sample at the coherence gate are sequentially acquired using a two-dimensional (2D) camera. It is performed by obtaining a plurality of images for a single interference map using the temporal phase-shifting method. As a consequence, the obtained information is highly susceptible to environmental vibrations and sample motion, which can cause phase errors or phase washout due to the long signal acquisition time of the phase-shifting process [7].

To address this drawback, recent studies have proposed an alternative technology called single-shot FF-OCT (S-FF-OCT) [8]. S-FF-OCT extracts sample information from the simultaneous acquisition of multiple phase-shifted interferograms, or even from a single interference acquisition,

#561708 https://doi.org/10.1364/BOE.561708
Journal © 2025 Received 7 Mar 2025; revised 9 Apr 2025; accepted 9 Apr 2025; published 18 Apr 2025

Biomedical Optics EXPRESS

enabling the observation of vibrating or moving samples. Several S-FF-OCT methods have been developed based on hyperspectral imaging [9], light polarization [8], and off-axis digital holography [10]. Among these methods, the polarization-based approach has been extensively studied for its systematic simplicity. It utilizes a polarization-sensitive Linnik interferometer with conventional polarization optics to generate three or four phase-shifted interferograms that are simultaneously captured using a single camera [8]. However, these systems require bulky and complicated phase-stepper optics, limiting their practical use [11,12].

In this study, we propose and demonstrate a simple and low-cost S-FF-OCT system that utilizes a single polarization camera as a detector. Single-sensor polarization cameras with integrated linear polarizers have been recently developed and are commercially available. They provide an easy and cost-effective method for acquiring polarization image information [13–15]. In a single-sensor polarization camera, a micro-polarizer array attached on the sensor plane consists of linear polarizers with different polarization orientations (0°, 45°, 90°, and 135°) repeated across the entire sensor area, creating polarization-sensitive pixels according to the polarization orientation. Each block of four pixels with different polarization orientations comprises a *superpixel*. From the ratios of the intensities measured by the four pixels in a superpixel, the camera can extract the polarization state for a polarization image [13–16]. In our proposed S-FF-OCT, the single-sensor polarization camera functions as a compact optical phase-stepper, yielding four quadrature phase-shifted interferograms in a single capture. By using a single camera, our method significantly reduces the form factor and systematic complexity. It also provides robust measurements against environmental perturbation and sample motion due to its single-shot signal acquisition. It is worth noting that the use of single-sensor polarization cameras in interferometric imaging has long been considered for a simple method of quantitative phase imaging [17]. Recent studies with commercialized polarization cameras have successfully demonstrated various phase imaging and surface topology measurements [18–21]. However, none has explored their application for FF-OCT based on the low-coherence imaging interferometry. In this report, we present the working principle and performance validation of our S-FF-OCT imaging method. In a single-shot imaging mode with a single camera-based configuration, our S-FF-OCT system was found to provide capabilities of sectional imaging, making it very suitable for *in vivo* dynamic imaging of microscopic objects.

2. Materials and methods

2.1. Proposed S-FF-OCT system

This section describes the operation principle of our S-FF-OCT method. Figure 1 shows a schematic of the proposed S-FF-OCT setup. The system utilizes a low-coherence Linnik interferometer and employs a 625 nm light-emitting diode (LED, M625L4, 700 mW, Thorlabs Inc.) as the light source. The LED has a spectral bandwidth of 17 nm at the full width at half maximum (FWHM), corresponding to a theoretical axial resolution of 10.14 µm. The unpolized light emitted from the LED, with an electric field randomly oscillating in all directions, passes through an aperture stop (AS) and a field stop (FS). The AS removes high spatial frequencies from the incident beam's wavefront, improving beam focusing performance by eliminating stray rays. The FS adjusts the beam size to control the field of view.

The unpolarized light is then filtered through a linear polarizer (P_{45}, LPVISC100-MP2, Thorlabs Inc.) tilted at 45° to the horizontal axis. This polarized light enters the Linnik interferometer, which consists of a non-polarizing beam splitter (BS) and a polarizing beam splitter (PBS). The PBS separates the incoming beam into orthogonal polarization states for the sample and reference arm. Each polarized beam is then focused by a pair of identical infinity-corrected 10× water-immersion microscope objective lenses (OBJs, UMPLFLN 10XW, 0.3 N.A., 18 mm focal length, Olympus) and reflected back from the sample and the mirror, respectively. The reflected beams are redirected to the single-sensor polarization camera (PCAM,

Biomedical Optics EXPRESS

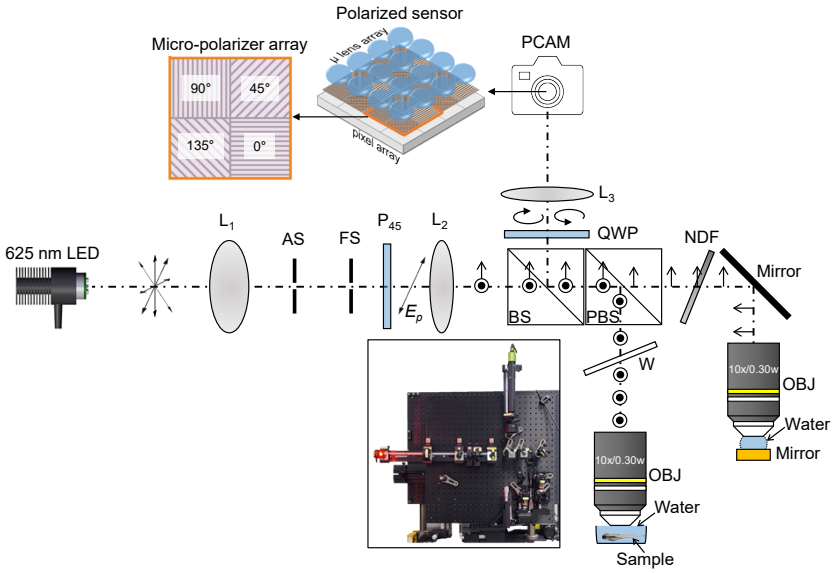

Fig. 1. Schematic of the proposed single polarization camera-based S-FF-OCT setup and its implementation (inset picture). AS, aperture stop; FS, field stop; P_{45}, 45° rotated linear polarizer; BS, beam splitter; PBS, polarizing BS; NDF, neutral density filter; W, window plate; OBJ, microscope objective, QWP, quarter wave plate; $L_{\#}$, lenses; PCAM, polarization camera.

GO-5100MP-USB, 2464 × 2056 pixels, 74 fps, 8 bits, JAI) via the PBS and the BS. A quarter-wave plate (QWP, AQWP05M-600, Thorlabs Inc.) tilted at 45° is placed before the PCAM to convert the polarization states of the reflected beams, which are then projected onto the sensor plane of the PCAM via a tube lens (L_3, 180 mm focal length). The system magnification is 10, determined by a ratio of the tube lens focal length (180 mm) to the OBJ focal length (18 mm). In addition, a neutral density filter (NDF) is obliquely placed in the reference arm to adjust the reference beam power. A transparent window plate, tilted at the same angle, is placed in the sample arm to compensate for the optical path length (OPL) change induced by the NDF.

The PCAM equips four different polarizers for a superpixel. They are tilted by 0°, 45°, 90°, and 135°, respectively. The four polarization-channeled images measure the intensities of the four different linearly polarized components. In order to find the intensities of the polarization channels, one can utilize the Jones matrix formalism. Just before the BS, the linearly polarized light denoted by $\mathbf{E}_p$ can be represented by the Jones vector:

$$\mathbf{E}_p = E_0 \begin{pmatrix} 1 \\ 1 \end{pmatrix}. \tag{1}$$

where E_0 is the field of the incident light. It has equal amplitudes in the x and y polarization axes. The PBS acts as a polarizer so that the light field in the sample arm is linearly polarized along the x polarization axis while that in the reference arm is polarized along the y polarization axis. For the light component of the sample arm, it experiences the PBS and the QWP. At the entrance of the PCAM, the Jones vector of the light field can be expressed as

$$\mathbf{E}_s = \frac{r_s E_0{}'}{4} e^{j(-\frac{\pi}{4})} \begin{pmatrix} 1+j \\ 1-j \end{pmatrix}. \tag{2}$$

Biomedical Optics EXPRESS

where r_s is the reflectance of the sample, and $E_0{}'$ is the light field delayed by the sample-arm path, respectively. Here, j is an imaginary unit. For the light component of the reference arm, it also experiences the PBS and the QWP. The Jones vector can be expressed as

$$\mathbf{E}_r = \frac{E_0{}''}{4} e^{j\left(-\frac{\pi}{4}\right)} \begin{pmatrix} 1-j \\ 1+j \end{pmatrix}. \tag{3}$$

where $E_0{}''$ is the light field delayed by the reference-arm path, respectively. If the relative delay between the sample arm and the reference arm is sufficiently larger than the coherence length of the incoherent light source, $E_0{}'$ and $E_0{}''$ are not correlated. The combination of the two orthogonal components, *i.e.*, $(\mathbf{E}_s + \mathbf{E}_r)$ is randomly polarized. Therefore, the four polarization channels will detect the same intensities. Otherwise, $E_0{}'$ and $E_0{}''$ are correlated so that the combined light field at the PCAM is polarized and becomes highly sensitive to the relative delay. When the relative delay is much smaller than the coherence length, the intensity of each channel can be easily found with the phase difference caused by the path-length difference. The channel-forming polarizer inside the PCAM is a linear polarizer tilted by θ =0°, 45°, 90°, or 135°. Its Jones matrix is expressed as

$$\mathbf{M}_\theta = \begin{pmatrix} \cos^2\theta & \cos\theta\sin\theta \\ \cos\theta\sin\theta & \sin^2\theta \end{pmatrix}. \tag{4}$$

Thus, the sample-originated light detected by a polarization channel of the PCAM is found as

$$\mathbf{E}_{s,\theta} = \frac{r_s E_0{}'}{4} e^{j\left(-\frac{\pi}{4}\right)} \mathbf{M}_\theta \begin{pmatrix} 1+j \\ 1-j \end{pmatrix}. \tag{5}$$

And the reference light detected by the same channel is expressed as

$$\mathbf{E}_{r,\theta} = \frac{E_0{}'}{4} e^{j\left(\Delta\varphi-\frac{\pi}{4}\right)} \mathbf{M}_\theta \begin{pmatrix} 1-j \\ 1+j \end{pmatrix}. \tag{6}$$

where $\Delta\varphi$ is the phase difference. The detected intensity for each channel is the squared absolutized norm of the combined light fields. For θ =0°, 45°, 90°, and 135°, respectively, the detected intensity of I_θ is obtained as

$$I_0 = I_{bg} + \frac{1}{4} r_s I \sin\Delta\varphi, \tag{7}$$

$$I_{45} = I_{bg} + \frac{1}{4} r_s I \cos\Delta\varphi, \tag{8}$$

$$I_{90} = I_{bg} - \frac{1}{4} r_s I \sin\Delta\varphi, \tag{9}$$

$$I_{135} = I_{bg} - \frac{1}{4} r_s I \cos\Delta\varphi. \tag{10}$$

where I_{bg} is a constant incoherent background intensity, and I is a constant of signal intensities. Equations (7)–(10) show that the intensities of the polarization channels form the phase-shifted interference quadrature with the common background intensity. The interference intensity of

Biomedical Optics EXPRESS

I_{int} can be obtained from those channel intensities in removing the background and the phase dependency as follows:

$$I_{\text{int}} \equiv \sqrt{(I_0 - I_{90})^2 + (I_{45} - I_{135})^2} = \frac{r_s I}{2}. \tag{11}$$

Eventually, one can extract the sample reflectivity of r_s from the interference intensity. It is worth noting it must assume a slowly varying signal of space. The sample-originated field must be the same for the four pixel elements within a superpixel. This can be achieved by optimizing the magnification of the image formation or limiting the aperture size.

2.2. System performance measurements

The performance of the phase-shifting interferometry was examined using a slightly tilted mirror as a test sample. Figure 2(a) shows four interference images of the tilted mirror surface captured by the PCAM. Each image (1252×1028 pixels corresponding to 533 μm (width) × 445 μm (height)) was generated by combining the interference signal pixels obtained through the 0°, 45°, 90°, and 135° polarizing filters. The intensities of the interference fringe patterns were measured along the white lines at the same position in all the images and plotted together, as shown in Fig. 2(b). The plot shows that the fringe waveforms in each line profile are almost equally shifted by $\lambda_0/4$, which is evident from the magnified view of the region enclosed by the box, where λ_0 is the center wavelength (625 nm) of the light source. This indicates that the system captures an ensemble of interference signals that are phase-shifted by 90° relative to one another in a single camera capture. Equation (11) was used with these interference signals to extract the sample reflectivity (FF-OCT signal), represented by the black solid line in Fig. 2(b), which corresponds to the background-eliminated envelope of the interference signal fringes. Consequently, an FF-OCT image (Fig. 2(c)) representing the extracted interferogram envelope was reconstructed from the phase-shifted interference images shown in Fig. 2(a). The periodic low-signal bands in Fig. 2(c) are visible due to the slight fringe structure on the envelope (Fig. 2(b)). These residual fringes may be observed in phase-shifting based fringe-envelope detection [4]. This can be attributed to imperfect phase shifts (ideally, $\pi/2$ for the central wavelength) between the interference images. Perfect elimination of the residual fringes is crucial for imaging samples with flat surfaces, such as microelectronics. However, it may be less critical for optical imaging inside biological media because the structures of biological samples are highly rough and irregular, and thus do not present the large, flat surfaces where residual fringes could be observed.

We evaluated the image resolution (axial (z) × transverse (x)) and sensitivity of the system. Briefly, the axial (z) resolution was estimated to be a 11.02 μm based on the width of the normalized point-spread function (PSF). This was measured from the central magnitudes of a stack of tomographic images of the mirror, recorded using a precision motorized stage with a step size of 1.8 μm (Supplement 1, Suppl. Fig. 1(a)). The resolution is slightly larger than the theoretical resolution of 10.14 μm, possibly due to optical aberrations between the two interferometer arms. To measure the transverse (x) resolution, we imaged a 1951 resolution test target, commonly used for determining the resolution of optical microscopes. The smallest line pairs (element 6, group 7) on the test target were distinguishable in the image, indicating that the transverse resolution was at least less than 4.38 μm (Supplement 1, Suppl. Fig. 1(b)). To measure the system sensitivity, we axially imaged the upper surface of a black glass plate with low reflectivity (0.15% at 620 nm), similar to the axial resolution measurement. The incident beam power was 280 μW. The axial PSF was plotted on a logarithmic scale (dB), and the signal was calibrated in reflectivity units. A background noise level of −74 dB was estimated, resulting in a dynamic range of approximately 48 dB (Supplement 1, Suppl. Fig. 1(c)). The dynamic range can be further improved by reducing the background noise through the accumulation of a greater number of images.

Biomedical Optics EXPRESS

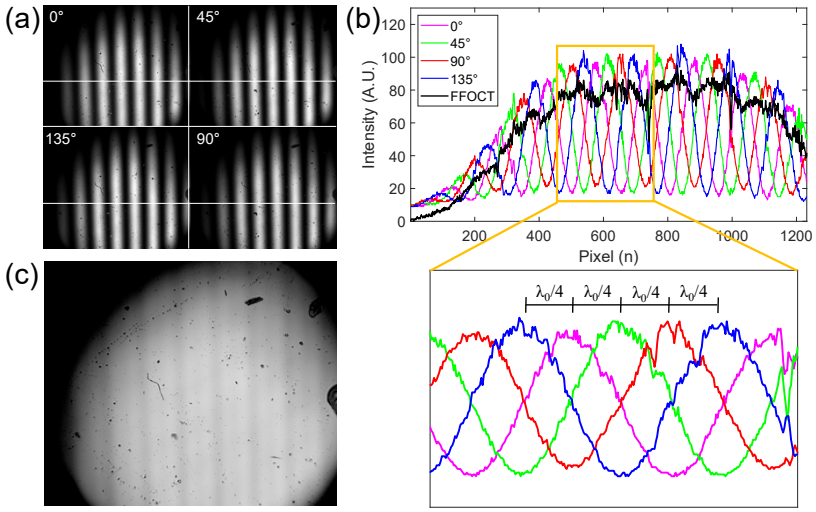

Fig. 2. Data acquisition and image reconstruction. (a) Four quadrature phase-shifted interference images of the tilted mirror surface, simultaneously captured by the polarization camera of the system. The interference images are generated by combining all the camera pixel intensities of the interference signals filtered by the polarizing filters with different rotation angles (indicated on the images) on the camera sensor. (b) Plot showing line profiles of the interference signal intensities obtained from the white lines on the images shown in (a). Magnified view of the region enclosed by the box in (b) shows the quadrature phase shifting between the interference signal fringes. We apply Eq. (11) to the line profiles to extract the background removed fringe envelop signal (black sold line in (b)), which represents the sample reflectivity referred to as the 'FF-OCT' signal. (c) FF-OCT image of the tilted mirror surface reconstructed from the images shown in (a).

3. Experimental results

3.1. S-FF-OCT imaging of a fast-moving object under vibration

We used the system to test the feasibility of vibration-insensitive FF-OCT imaging of a scattering object. The system was exposed to an environment with background vibrations in the 1–200 Hz frequency range, encompassing most sources of acoustic, machinery, and building vibrations in a typical laboratory. A plastic credit card was mounted on a motorized translation stage (MTS25-Z8, Thorlabs Inc.). A hologram on the card (indicated by the red box in Fig. 3(a)) was then imaged while the stage was horizontally moved at a speed of 0.5 mm/s. The camera frame rate and exposure time were set to 74 fps and 5 ms, respectively. Figure 3(b) shows the FF-OCT image (3.2 mm (width) × 0.45 mm (height)) of the hologram, created by mosaicking 12–13 S-FF-OCT images (533 µm (width) × 445 µm (height)) acquired along the movement direction (arrow). The microstructural details of the hologram on the card were clearly delineated (see insets) without afterimages, even though the object was moving at a stage velocity of 0.5 mm/s (Visualization 1) and 1.0 mm/s (Fig. 3(c), Visualization 2). Additionally, S-FF-OCT imaging of other fast-moving samples (lens cleaning tissues) in axial and arbitrary directions was demonstrated (Visualization 3 and Visualization 4). These results indicate the feasibility of high-resolution FF-OCT imaging and monitoring of static or mobile samples exposed to external vibrational noise.

Biomedical Optics EXPRESS

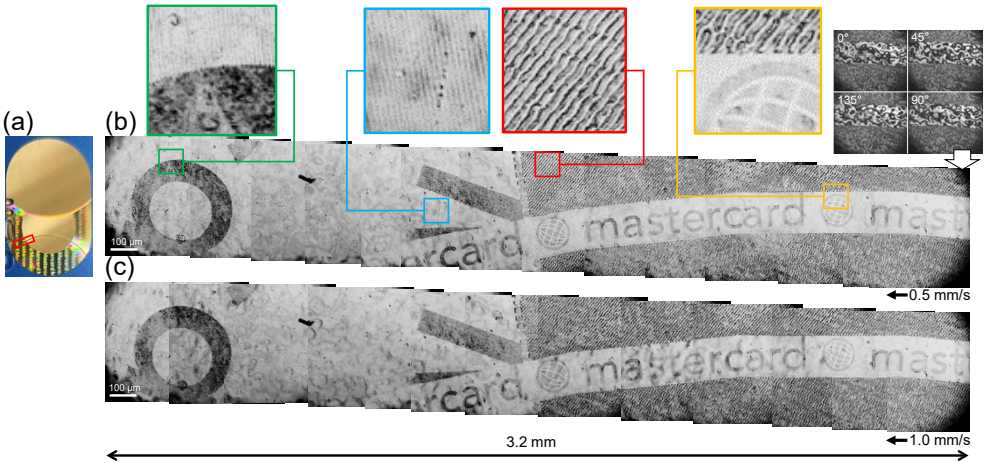

Fig. 3. S-FF-OCT imaging test of the sample in motion under vibration. Measurements were carried out with the hologram on plastic card translated by a moving platform. (a) Photograph of the hologram. Imaging area is indicated by the red box. (b) FF-OCT image (3.2 mm (width) × 0.45 mm (height)) of the moving hologram. Mosaic of multiple FF-OCT images of the sample was laterally moved at a velocity of 0.5 mm/s relative to the system. Insets clearly exhibit morphological details of the hologram. (c) FF-OCT image of the same region of the hologram at a faster speed (1.0 mm/s).

3.2. *Depth-resolved S-FF-OCT imaging of scattering objects*

We examined the tomographic capabilities of our system using several scattering samples. Similar to Sec. 3.1, the system was used under ambient vibration conditions. First, we imaged stacked cover glasses (Fig. 4(a)), serving as simple layered weak scattering samples, by vertically moving them towards the OBJ in the sample arm. Figure 4(b) shows a bright-field microscope image of the illuminated area of the sample, including two separate water-based ink spots: one (spot1) on the upper surface of the first glass and another (spot2) on the upper surface of the lower glass. A conventional microscope cannot image the two upper layers in depth due to the lack of coherence gating. However, our system enables the visualization of these glass layers at different depths, as shown in Figs. 4(c) and 4(d). The concentric interference patterns on the spots may be due to the self-interference between the curved surface of the spot and the flat glass surface below.

Depth-resolved imaging was also performed on different turbid media containing living biological samples. The power of the beam incident on the samples was adjusted to below 100 µW for highly reflective materials and 280 µW for biological samples. Figures 4(e) and 4(f) show FF-OCT images of the front of the plastic card on the surface ($z = 0$ µm) and at a depth of 40 µm from the surface, respectively. Based on the composition of the credit card, Fig. 4(e) shows the top surface of an overlay layer made from transparent polyvinyl chloride (PVC), and Fig. 4(f) reveals the PVC grains (particles) within the overlay layer [22]. Figures 4(g) and 4(h) show FF-OCT images of an onion on the surface and at a depth of 30 µm from the surface, respectively. These images depict typical subsurface cellular anatomy of the onion, including onion cells, cell walls and cytoplasm. A similar morphology to that of the onion is observed in the FF-OCT image of a banana peel, which exhibits an epidermis consisting of a single layer of small, elliptical cells (Fig. 4(i)) and subsequent hexagonal cellular structures (Fig. 4(j)). A two-day-old guppy fry (inset in Fig. 4(k)) was prepared for FF-OCT imaging as a living biological specimen. Prior to measurement, the fish was immersed in cold water at 4 °C for 30 seconds to reduce its movement during the imaging (the imaging area is indicated by the box in the inset). Figures 4(k) and 4(l) show FF-OCT images of the lateral skin tissue of the fish body and the interior of an organ, which

Biomedical Optics EXPRESS

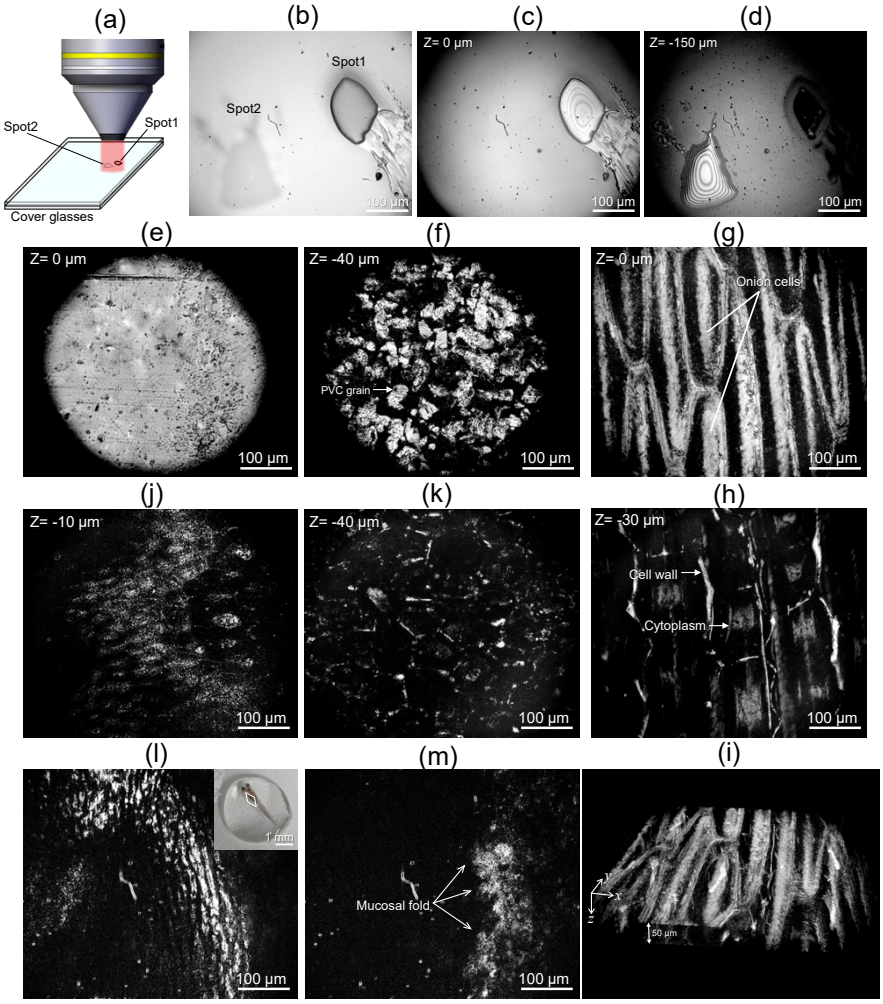

Fig. 4. Depth-resolved S-FF-OCT imaging of several scattering samples. (a) Illustration of the simple layered sample (a stack of two cover glasses with ink spots stained on the upper surfaces of the top and bottom glasses) illuminated by the OBJ in the sample arm. (b) Bright-field microscope image of the illuminated sample area. (c) FF-OCT image of the sample shown in (b) at $z = 0$ and (d) $z = -150\,\mu m$. The spots at the different layer depths are identified. (e) FF-OCT image of the plastic card at $z = 0$ and (f) $z = -40\,\mu m$. The particles shown in (f) may be PVC grains in the transparent overlay layer of the card shown in (e). FF-OCT images of an onion at $z = 0$ (g) and $z = -30\,\mu m$ (h), showing typical cellular compositions of the onion surface and subsequent interior. (i) 3D reconstruction of the depth-resolved onion images. FF-OCT images of a banana peel at $z = 0$ (j) and $z = -40\,\mu m$ (k). (l, m) FF-OCT images of biological specimen (guppy fry two days after hatching), obtained from the sample during swimming (see inset in (l)). The images show the skin tissue in (l) and the inner structure below the skin (m), which is speculated to be a part of the digestive tract such as the stomach.

Biomedical Optics EXPRESS

is speculated to be the digestive tract [23]. As the fish body is largely oval and non-uniform, only a small portion of the skin tissue is imaged within the flat coherent gate. The imaging results demonstrate the ability of our system to visualize the microanatomy of various samples *in situ*.

4. Discussion and conclusion

This study has proposed and implemented a novel design for FF-OCT with no moving parts, referred to as Single-shot FF-OCT (S-FF-OCT). Compared to existing S-FF-OCT methods, the proposed method uses a commercially available, low-cost, single-sensor polarization camera as the detector of a polarization-sensitive Linnik interferometer. This acts as a spatial optical phase stepper to achieve snapshot phase-shifting interferometry. This functional approach represents the first attempt at S-FF-OCT using a polarization camera, resulting in a system that is simple, compact (in terms of configuration and form factor), and cost-effective. The system was used to demonstrate S-FF-OCT imaging performance for various stationary and mobile scattering samples in environments with vibration. The system has the potential to be a versatile, non-invasive, and *in situ* imaging technique for a broad range of applications in fields including biomedicine and industry.

In addition, our system can provide the optical phase $\Delta\varphi$ in the interferometric signals, which can be extracted as

$$\Delta\varphi = \tan^{-1}\left|\frac{I_0 - I_{90}}{I_{45} - I_{135}}\right|. \tag{12}$$

Since $\Delta\varphi$ includes optical path-length difference (OPD) between the sample arm and the reference arm, this phase information can offer the sample displacement relative to the reference arm with subwavelength accuracy [24]. This capability would be useful for measuring nanometer scale surface topology or monitoring subtle optical changes within the sample media. We tested the phase measurement of a biological sample (human hair) with our system and the results are shown in Fig. 5. Note that the 10× objectives were replaced by higher magnification (40×) objectives with a focal length of 4.5 mm for hair imaging. Figure 5(a) shows a FF-OCT image at the surface of a hair shaft plucked from a healthy young male subject. Figure 5(b) is a phase map of Fig. 5(a), wrapped within 2π modulo. After unwrapping, the phase map ($\Delta\varphi$) is unfolded (Fig. 5(c)), from which OPDs ($\Delta d = \frac{\lambda_0 \Delta\phi}{4}$) are extracted and displayed as a hair surface topology (Fig. 5(d)). The results indicate the feasibility of phase imaging with our system, which will be utilized in future studies.

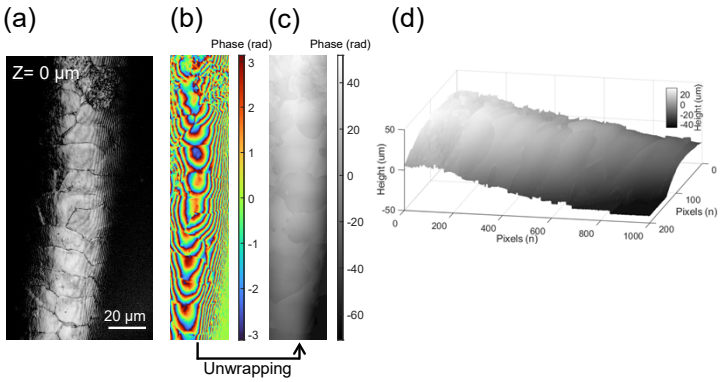

Fig. 5. Phase measurement of a biological sample with S-FF-OCT. (a) FF-OCT image at the surface of a human hair shaft. (b) Wrapped phase map of (a), extracted from Eq. (12). (c) Unwrapped phase map. (d) OPDs extracted from (c), representing a surface topology of the hair shaft.

Biomedical Optics EXPRESS

Despite the successful implementation and promising results, certain limitations still exist. One major challenge is the difficulty in imaging birefringent materials. Unlike isotropic turbid media, linearly birefringent turbid media modulate the polarization of light propagating through them [25]. Birefringence is particularly prevalent in biological tissues, such as collagen or muscle, and results from the linear anisotropy of fibrous structures [26]. Therefore, the polarization state of light backscattered from the birefringent tissue in the sample arm of the system may be altered from its initial state, which can induce errors in the phase shift measurements. This can result in critical residual fringes and potential background signals in the FF-OCT images [27]. This measurement error may be reduced if the reference and sample beams are circularly polarized rather than linearly polarized [27]. Alternatively, the error may be resolved by applying the mathematical Hilbert transform to only two of the four phase-shifted interferograms [28], from which the sample information can be retrieved regardless of the phase error.

This study used a 625 nm LED source with a narrow bandwidth (17 nm), yielding an axial resolution of ~11 μm. However, this is not sufficient for resolving micrometer scale structures in depth. The axial resolution can be improved using spectrally broad (more than 200 nm at FWHM) light sources such as white LEDs or tungsten-halogen light sources. The polarization optics in our system maintain an extinction ratio of at least 1000:1 over the full operating bandwidth (510-800 nm). Given that an extinction ratio of 1000:1 or higher is typically considered sufficient for high-contrast polarization in the desired direction, the current polarization optics would also be suitable for broadband light sources, potentially achieving axial resolution down to the sub-micrometer range.

Another issue is the mismatch between interference images in a single capture, attributed to the geometry of the polarizer array in the camera. The positions of the four polarizing pixel elements partitioned in the superpixel are physically different. Therefore, the four camera images formed by pixel elements with the same polarization are not perfectly registered but appear to be laterally shifted with respect to each other by at least the pixel size (3.45 μm). This location disparity may be critical for FF-OCT image reconstruction because it generates noticeable background artifacts in FF-OCT images due to the intensity differences at the corresponding pixels. However, the artifacts were marginal in this study. This may be because the 10× and 40× OBJs in the system magnified the PSFs of the object to more than 11 μm, which is much larger than the superpixel, thus, leading to an oversampling effect.

In conclusion, S-FF-OCT imaging is a natural progression of *in situ* FF-OCT technologies. In this regard, the proposed S-FF-OCT technique is a practical choice owing to its simplicity and cost-effectiveness. We expect that this technology will be widely utilized as a non-invasive imaging tool for on-site measurement and inspection of various microscopic samples.

Funding. National Research Foundation of Korea (NRF-2021R1A2C1004526,RS-2020-NR049537,RS-2023-NR076420); Korea Institute for Advancement of Technology (P0020967).

Disclosures. The authors declare no conflicts of interest.

Data availability. The data supporting the results of this study are available from the corresponding author upon reasonable request.

Supplemental document. See Supplement 1 for supporting content.

References

1. B. E. Bouma, J. F. de Boer, D. Huang, *et al.*, "Optical coherence tomography," Nat. Rev. Methods Primers **2**(1), 79 (2022).
2. G. Fujimoto, C. Pitris, S. A. Boppart, *et al.*, "Optical coherence tomography: an emerging technology for biomedical imaging and optical biopsy," Neoplasia **2**(1-2), 9–25 (2000).
3. M.-Y. Fu, Z.-H. Yin, X.-Y. Yao, *et al.*, "The progress of optical coherence tomography in industry applications," Adv. Devices Instrum. **5**, 1 (2024).
4. A. Dubois, K. Grieve, G. Moneron, *et al.*, "Ultrahigh-resolution full-field optical coherence tomography," Appl. Opt. **43**(14), 2874–2883 (2004).

Biomedical Optics EXPRESS

5. L. Wang, R. Fu, C. Xu, *et al.*, "Methods and applications of full-field optical coherence tomography: a review," J. Biomed. Opt. **27**(05), 050901 (2022).
6. S. Chang, X. Cai, and C. Flueraru, "An efficient algorithm used for full-field optical coherence tomography," Opt. Lasers Eng. **45**(12), 1170–1176 (2007).
7. P. J. de Groot, "Vibration in phase-shifting interferometry," J. Opt. Soc. Am. A **12**(2), 354–365 (1995).
8. H. M. Subhash, "Full-field and single-shot full-field optical coherence tomography: a novel technique for biomedical imaging applications," Adv. Opt. Technol. **2012**(2012), 1–26 (2012).
9. R. R. Iyer, M. Zurauskas, Q. Cui, *et al.*, "Full-field spectral-domain optical interferometry for snapshot three-dimensional microscopy," Biomed. Opt. Express **11**(10), 5903–5919 (2020).
10. E. M. Seromenho, A. Marmin, S. Facca, *et al.*, "Single-shot off-axis full-field optical coherence tomography," Appl. Phys. Lett. **121**(11), 113702 (2022).
11. M. Zurauskas, R. R. Iyer, and S. A. Boppart, "Simultaneous 4-phase-shifted full-field optical coherence microscopy," Biomed. Opt. Express **12**(2), 981–992 (2021).
12. C. Dunsby, Y. Gu, and P. French, "Single-shot phase-stepped wide-field coherence-gated imaging," Opt. Express **11**(2), 105–115 (2003).
13. N. Hagen and Y. Otani, "Using polarization cameras for snapshot imaging of phase, depth and spectrum," Opt. Rev. **31**(4), 359–368 (2024).
14. D. Gottlieb and O. Arteaga, "Mueller matrix imaging with a polarization camera: application to microscopy," Opt. Express **29**(21), 34723–34734 (2021).
15. E. Bruggeman, O. Zhang, L.-M. Needham, *et al.*, "POLCAM: instant molecular orientation microscopy for the life sciences," Nat. Methods **21**(10), 1873–1883 (2024).
16. X. Wu, C. Fan, X. He, *et al.*, "Bionic orientation method based on polarization imaging in HDR scenes," Appl. Opt. **61**(8), 2007–2018 (2022).
17. K. Creath and G. Goldstein, "Dynamic quantitative phase imaging for biological objects using a pixelated phase mask," Biomed. Opt. Express **3**(11), 2866–2880 (2012).
18. J. W. Jeon and K.-N. Joo, "Single-shot imaging of two-wavelength spatial phase-shifting interferometry," Sensors **19**(23), 5094 (2019).
19. S. Cui, S. Gao, C. Li, *et al.*, "Quantitative phase imaging based on polarization encoding," Opt. Express **30**(24), 43622–43632 (2022).
20. M. Strassberg, Y. Shevtsova, D. Kamel, *et al.*, "Single-shot quantitative phase imaging with polarization differential interference contrast," Appl. Phys. Lett. **119**(17), 173702 (2021).
21. S. Liu, C. Zheng, Q. Hao, *et al.*, "Single-shot quantitative differential phase contrast imaging combined with programmable polarization multiplexing illumination," Opt. Lett. **48**(13), 3559–3562 (2023).
22. R. Darvishi and A. Shahi, "The effects of initiators mixture on suspension polymerization of vinyl chloride and its comparison with other productivity-enhancing procedures," Int. J. Plast. Technol. **23**(2), 146–156 (2019).
23. J.-H. Cho, J. W. Park, Y.-W. Ryu, *et al.*, "Morphology, histology, and histochemistry of the digestive tract of the marbled flounder *pseudopleuronectes yokohame*," Animals **13**(5), 936 (2023).
24. A. Dubois, "Phase-map measurements by interferometry with sinusoidal phase modulation and four integrating buckets," J. Opt. Soc. Am. A **18**(8), 1972–1979 (2001).
25. X. Wang and L. V. Wang, "Propagation of polarized light in birefringent turbid media: time-resolved simulations," Opt. Express **9**(5), 254–259 (2001).
26. S. K. Nadkarni, M. C. Pierce, B. H. Park, *et al.*, "Measurement of collagen and smooth muscle cell content in atherosclerotic plaques using polarization-sensitive optical coherence tomography," J. Am. Coll. Cardiol. **49**(13), 1474–1481 (2007).
27. C. Zhao, D. Kang, and J. H. Burge, "Effects of birefringence on Fizeau interferometry that uses a polarization phase-shifting technique," Appl. Opt. **44**(35), 7548–7553 (2005).
28. J. Na, W. J. Choi, E. S. Choi, *et al.*, "Image restoration method based on Hilbert transform for full-field optical coherence tomography," Appl. Opt. **47**(3), 459–466 (2008).